CME LIVE OPEN ACCESS

Engineering and Applied Sciences Journal

Research Article ISSN: 3067-8005

Moiré Period in Volumetric Moiré Effect with Refraction

Vladimir Saveljev*

Independent Researcher, Daejeon, South Korea.

***Corresponding Author:** Vladimir Saveljev, Independent Researcher, Daejeon, South Korea.

Received: 2026 Sep 16 **Accepted:** 2026 Oct 16 **Published:** 2026 Oct 25

Abstract

We investigated the moiré effect in a volumetric rectangular container while accounting for refraction. We derived an analytical solution that defines the moiré period as a function of distance, based on projections observed from different viewpoints. We proposed a method for calculating the effective root-mean-square deviation (RMSD) for curves with steep tangent angles. This work provides deeper insight into the physical nature of the moiré effect in rectangular objects with refraction. The findings have potential applications in advertising, as well as in measuring refractive indices or liquid levels.

Keywords: Moiré Effect, Moiré Phenomenon, Moiré Refraction, Volumetric Object, Central Projection, Root-Mean-Square Deviation

1. Introduction

The moiré effect is a physical phenomenon that occurs when periodic or nearly periodic structures or their projections are superimposed. It is an incoherent nonlinear interference. Moiré patterns appear as relatively wide stripes [1,2]. Researchers typically study the moiré effect in systems with coplanar layers [3-5]. This effect has also been studied in layers separated by a gap in hollow three-dimensional objects (such as shells), and in nanoparticles [6-13]. The moiré effect in connection with refraction was discussed in [14-17]. In the current paper, we investigated the moiré effect in a volumetric object (a rectangular parallelepiped) while accounting for light refraction within an improved theoretical framework. This represents a step toward studying the dynamic moiré effect in filled containers of various shapes.

We also proposed a method for calculating the effective root-mean-square deviation (RMSD) for curves with steep tangent angles. Unlike the standard RMSD, whose calculation includes only vertical deviation (Δy), our method utilizes the shortest distance from experimental points to the theoretical curve (effectively accounting for both Δx and Δy), a critical factor for curves of this type. The discrepancy with experimental data is several times better than results reported in previous studies of the moiré effect involving refraction. The article is organized as follows. Section 2 describes the theoretical principles. Section 3 presents the theory (formulas for the projection coefficient and the moiré magnification coefficient, accounting for refraction) and compares the theoretical results with experimental data. Section 4 contains a brief discussion, and Section 5 concludes the article.

2. Materials and Methods

The moiré wavenumber is equal to the difference of the wavenumbers of two grids projected onto the same screen [1,2].

$$k_M = k'_2 - k'_1 \tag{1}$$

where k_M is the moiré wavenumber k_1 and k_2 are the grid wavenumbers, and the prime sign denotes projection. According to this formula, the moiré wavenumber may be signed, i.e., positive or negative. The first grid is the one nearest camera. We characterize the moiré patterns in terms of the signed moiré magnification coefficient (gain), which is equal to the ratio of the moiré wavenumber to the wavenumber of the first grid,

$$\mu = \frac{k_1}{k_M} \tag{2}$$

For positive values of periods, the modulus of the gain coefficient is

$$|\mu| = \frac{\lambda_M}{\lambda_1} \tag{3}$$

where λ_M is the period of the moiré patterns, and λ_1 and λ_2 are grid periods.

This coefficient can be used instead of the period when the moiré period is linearly proportional to the grid period, as in the current problem.

The ratio of grid periods ρ is defined as

$$\rho = \frac{\lambda_2}{\lambda_1} \tag{4}$$

The origin is at the geometric center of the rectangular container (box). The screen is at the origin, as shown in Fig. 1.

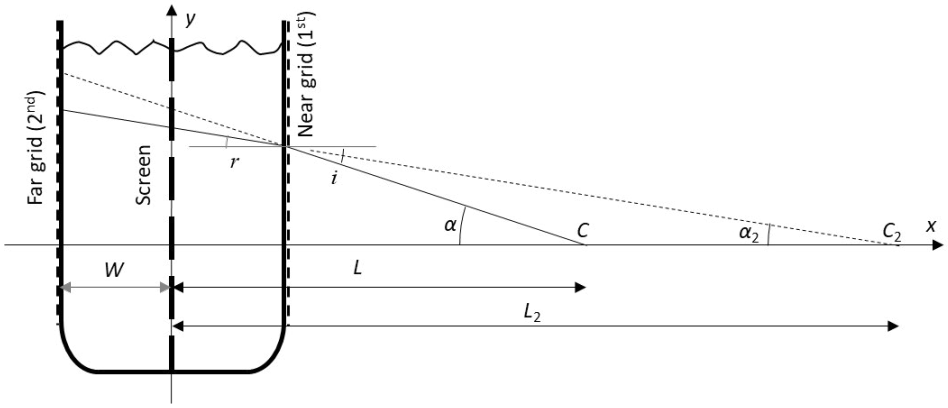


Figure 1: Rectangular Container with Grids on Its Sides

The physical center of projection (observer or camera) is located at C. Note the additional, virtual center of projection C_2. The direction of the camera axis is opposite to the x-axis.

For convenience, we define the relative quantity,

$$\hat{L} = \frac{L}{W} \tag{5}$$

where L is the distance to the camera, and W is the half-width of the box (along the camera axis). The ordinate (y) in the near plane projected onto the origin can be obtained (either from the similar triangles in this particular geometry or using the homogeneous projection matrix in the general case [18] as follows.

$$y' = y\frac{\hat{L}}{\hat{L}-1} \tag{6}$$

where λ is the period of the grid, and λ' is its period projected onto the screen. Equation (6) transforms the lateral coordinates. Because of the linear proportionality and the fact that the far surface is perpendicular to the camera axis, the projected period is equal to

$$\lambda' = \lambda\frac{\hat{L}}{\hat{L}-1} \tag{7}$$

(Note that in the current geometry, this is equivalent to differentiation with respect to the lateral coordinate, as suggested in [19-20]). The value of $\frac{\hat{L}}{\hat{L}-1}$ characterizes the projection of the period and can be named a projection coefficient for the period of the grid, so as

$$\mathfrak{M} = \frac{\lambda'}{\lambda} \tag{8}$$

Accordingly,

$$\lambda' = \mathfrak{M}\lambda \tag{9}$$

For the near grid, the projection coefficient is

$$\mathfrak{M} = \frac{\hat{L}}{\hat{L}-1} \tag{10}$$

In the absence of refraction, the projection coefficient of the far grid can be obtained from Eq. (10) by replacing $\hat{L}-1$ by $\hat{L}+1$. If refraction is present, additional calculations are required; see Sec. 3. Snell's law for arbitrary angles is:

$$\sin r = \frac{\sin i}{n} \tag{11}$$

where i is the angle of incidence, and r is the angle of refraction.

We use the approximation of small angles (within the angular range of ±18°), and Snell's law for small angles looks like this:

$$r = \frac{i}{n} \tag{12}$$

We consider $\mathfrak{M}$ and μ as functions of the distance, while other quantities (ρ, n, etc.) are parameters denoted in formulas by sub- and superscripts. Note that $\hat{L}$, $\mathfrak{M}$ and μ are dimensionless quantities, i.e., numbers without measurement units.

3. Results

3.1 Projection Coefficient with Refraction

The tangents of the view angles of the camera are:

$$\tan\alpha = \frac{y_0}{\hat{L}-1} \tag{13}$$

$$\tan\alpha_2 = \frac{y_0}{\hat{L}_2 - 1} \tag{14}$$

For small angles, the tangents become

$$\alpha = \frac{y_0}{\hat{L} - 1} \tag{15}$$

$$\alpha_2 = \frac{y_0}{\hat{L}_2 - 1} \tag{16}$$

The angles of incidence and refraction are

$$i = \alpha \tag{17}$$

$$r = \alpha_2 \tag{18}$$

So, by Snell's law,

$$\alpha_2 = \frac{\alpha}{n} \tag{19}$$

Excluding y_0 from the Eqs. (15) and (16) for tangents, we can find $\hat{L}_2$:

$$\hat{L}_2 = n(\hat{L} - 1) + 1 \tag{20}$$

So, we have for the projection of the far grid onto the origin using C_2,

$$y_2' = y_2 \frac{\hat{L}_2}{\hat{L}_2 + 1} = y_2 \frac{n(\hat{L} - 1) + 1}{n(\hat{L} - 1) + 2} \tag{21}$$

Equation (21) transforms coordinates. Similarly, to Eqs. (6) and (7), the projected period equals

$$\lambda_2' = \lambda_2 \frac{n(\hat{L} - 1) + 1}{n(\hat{L} - 1) + 2} \tag{22}$$

Thus, the projection coefficient for the period (period magnification) of the far grid accounting for refraction is as follows,

$$\mathfrak{M} = \frac{n(\hat{L} - 1) + 1}{n(\hat{L} - 1) + 2} \tag{23}$$

Figure 2 shows the function.

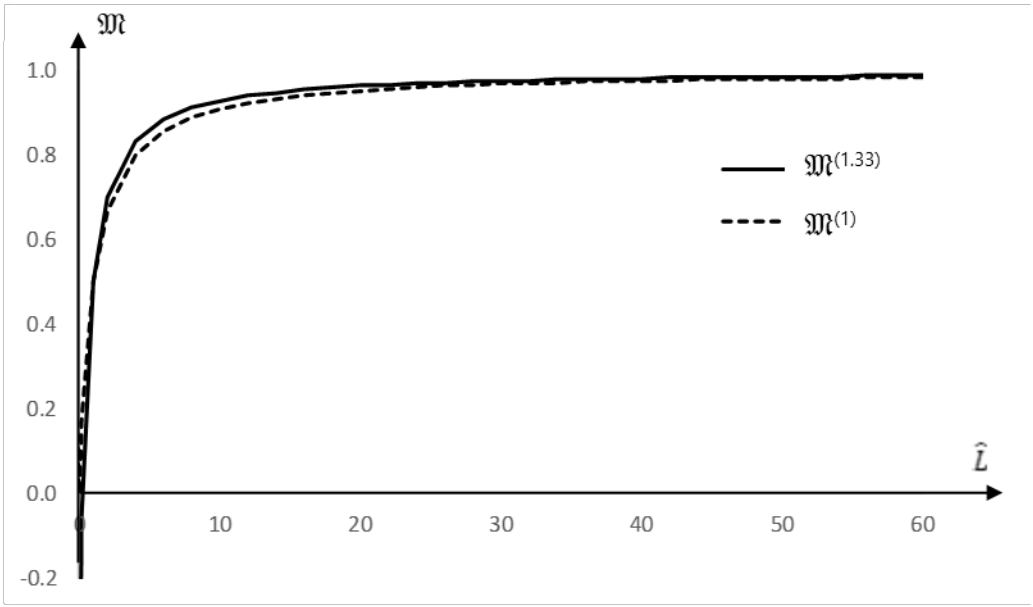


Figure 2: Theoretical Projection Coefficient $\mathfrak{M}$ in Air and Water as a Function of Distance.

Particular Cases

At $\hat{L} = 1$ and at infinity (in both air and water),

$$\mathfrak{M}(1) = \frac{1}{2} \tag{24}$$

$$\mathfrak{M}(\infty) = 1 \tag{25}$$

In air (n =1),

$$\mathfrak{M}^{(1)} = \frac{\hat{L}}{\hat{L} + 1} \tag{26}$$

as expected.

3.2 Moiré Magnification

The period of the first (near) grid onto the screen at the origin can be obtained from Eq. (9),

$$\lambda_1' = \mathfrak{M}^{(1)}\lambda_1 \tag{27}$$

and

$$k_1' = \frac{k_1}{\mathfrak{M}^{(1)}} \tag{28}$$

The projected k_2 can be obtained using the projection coefficient with refraction $\mathfrak{M}$ in Eq. (23),

$$k_2' = \frac{k_2}{\mathfrak{M}} = k_2 \frac{n(\hat{L}-1)+2}{n(\hat{L}-1)+1} \quad (29)$$

The moiré wavenumber based on the fundamental formula Eq. (1) is

$$k_m = k_2 \frac{n(\hat{L}-1)+2}{n(\hat{L}-1)+1} - k_1 \frac{\hat{L}-1}{\hat{L}} =$$

$$= \frac{k_1}{\rho} \frac{n(1-\rho)\hat{L}^2 + \big(2-n+\rho(2n-1)\big)\hat{L} - \rho(n-1)}{\hat{L}(n\hat{L}-n+1)} \quad (30)$$

The corresponding moiré magnification for the screen at the origin is

$$\mu = \frac{\rho\hat{L}(n\hat{L}-n+1)}{n(1-\rho)\hat{L}^2 + \big(2-n+\rho(2n-1)\big)\hat{L} - \rho(n-1)} \quad (31)$$

Particular cases.
At $\hat{L}=1$,

$$\mu(1) = \frac{\rho}{2} \quad (32)$$

At infinity (in both air and water),

$$\mu(\infty) = \frac{\rho}{1-\rho} \quad (33)$$

as in [21]; for ρ = 1.09, it equals -12.1.

The moiré magnification is infinite when the denominator of Eq. (31) is zero, i.e., when

$$n(1-\rho)\hat{L}^2 + \big(2-n+\rho(2n-1)\big)\hat{L} - \rho(n-1) = 0 \quad (34)$$

The roots of the square equation are

$$\hat{L}_\infty = \frac{-\big((2-n)+\rho(2n-1)\big) \pm \sqrt{(2-n)^2 + 2(3n-2)\rho + \rho^2}}{2n(1-\rho)} \quad (35)$$

Particularly, in air,

$$\hat{L}_\infty^{(1)} = \frac{-(1+\rho) \pm (1+\rho)}{2(1-\rho)} \quad (36)$$

which gives two roots

$$\hat{L}_\infty^{(1)} = 0, \qquad \frac{\rho+1}{\rho-1} \quad (37)$$

and the second root coincides with that in [21].
In water,

$$\hat{L}_\infty^{(1.33)} \approx \frac{-(2+5\rho) \pm \sqrt{4+36\rho+9\rho^2}}{8(1-\rho)} \quad (38)$$

The denominator is similar to $\hat{L}_\infty^{(w)} = \frac{\rho+0.5}{\rho-1}$ [21]. Numerically (for ρ = 1.09), the roots are:

$$\hat{L}_\infty^{(1.33)} = 1.15,\ \ 20.55$$

$$\hat{L}_\infty^{(1)} = 0.0,\ \ 23.22$$

Figure 3 shows the graphical illustration. Note that the peaks near zero are very narrow.

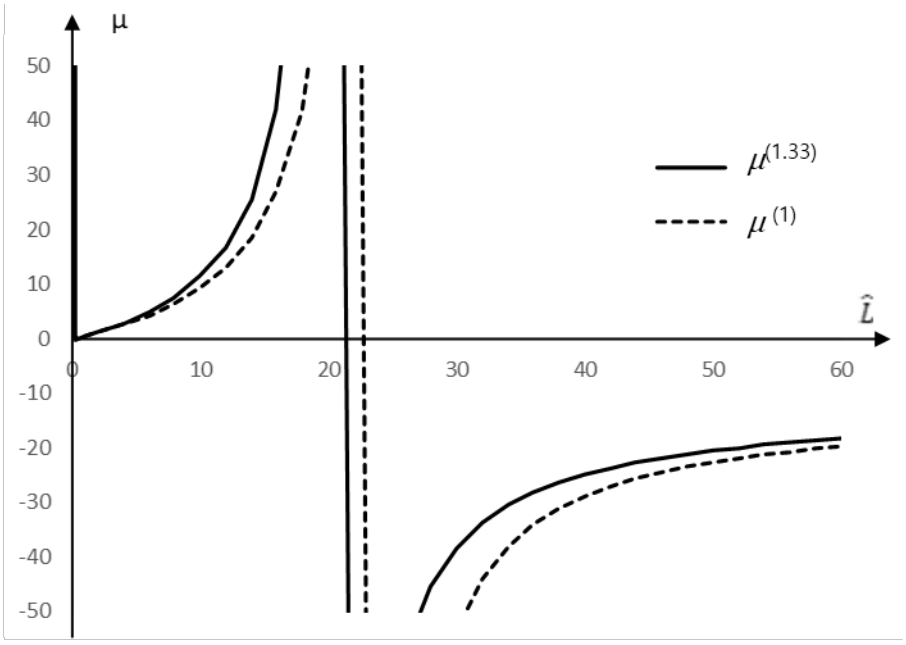


Figure 3: Theoretical Moiré Magnification μ in Air and Water for ρ = 1.09

Particular cases.
Identical grids:

$$\mu_{(=)} = \frac{\hat{L}(n\hat{L} - n + 1)}{\hat{L} + (n\hat{L} - n + 1)} \quad (39)$$

In air (n = 1),

$$\mu^{(1)} = \frac{\rho\hat{L}}{(1-\rho)\hat{L} + (1+\rho)} \quad (40)$$

This case is identical to [21].

3.3 Comparison with Experiment

Whereas the theoretical μ is a signed function (positive somewhere and negative elsewhere), the measured period is always positive by its physical meaning. Therefore, we compared the modulus of the theoretical function $|\mu|$ with the relative moiré period measured in experiments. Namely, we compared the existing experimental data with the proposed theory. Figure 4 shows the theoretical and experimental moiré period in air and water (label "TH water" means the theory in Ref. [21], "TH water+" the theory presented here).

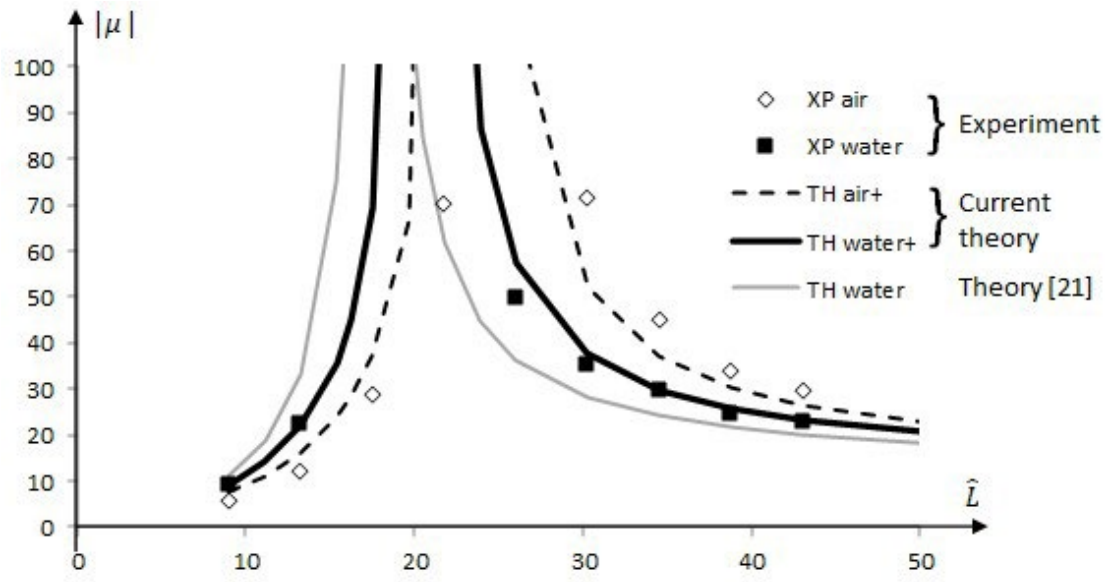


Figure 4: The Current Theory Compared with Experiment and Theory [21]

The normalized RMSD with the proposed theory is 7.1% and 4.7% in air and water, resp., compared with 19.4% and 26.4% in Ref. [21], i.e., the theory's reliability improved by 7.3- and 5.6-fold. However, the standard RMSD calculation procedure does not seem appropriate for curves with steep tangent angles near the theoretically infinite maximum. The regular procedure includes only the vertical deviation (Δy). The discrepancy is clear in Fig. 4 for values in air: their Δy is very large, whereas the Euclidean distance to the theoretical curve is not. To make comparison more appropriate, our method utilizes the shortest distance from experimental points to the theoretical curve along the curve's normal (effectively accounting for both Δx and Δy)—a critical factor for curves of this type. The proposed calculation of the effective RMSD is based on the minimized distance from the experimental point to the theoretical curve, which was calculated in Python using the function scipy. optimize. minimize() with the objective function of the square root (representing the Euclidean distance) [22].

$$d = \sqrt{\left(x_{exp} - x_{theor}\right)^2 + \left(y_{exp} - y_{theor}\right)^2} \quad (41)$$

Figure 5 shows the calculated nearest points for the left and right branches of the function separately.

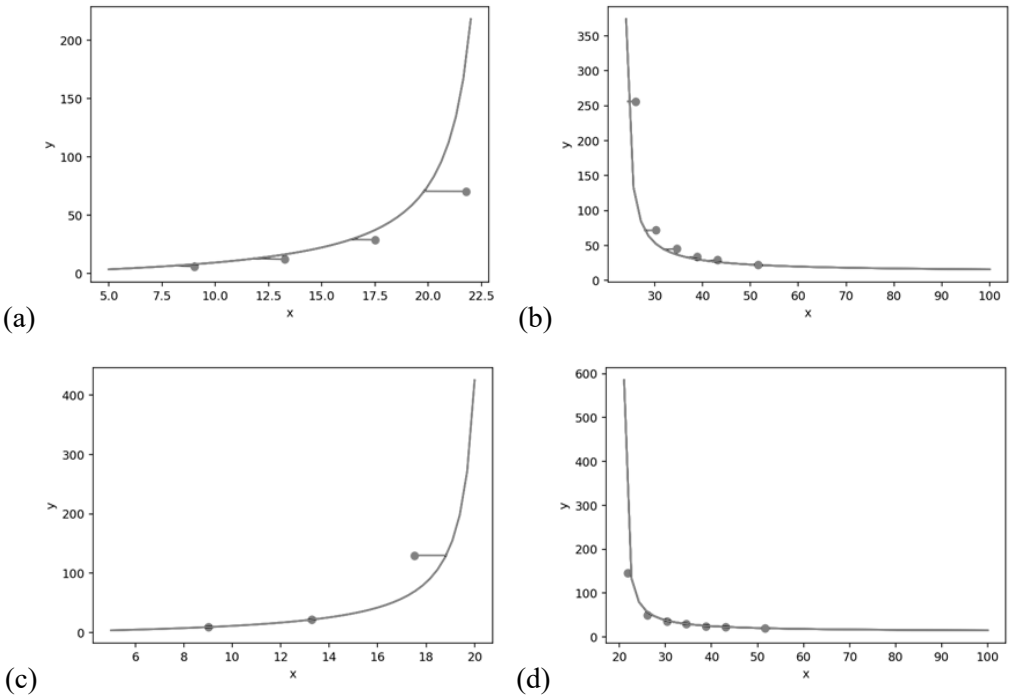


Figure 5: Nearest Points: (a) and (b) in Air; (c) and (d) in Water

The position of the nearest points in Figs. 5(a) and (c) look somewhat strange, but this is because of improper scales in Fig. 5 (note the difference in numbers on the abscissa and ordinate). For illustration, Fig. 6(b) redraws one branch with the identical horizontal and vertical scales.

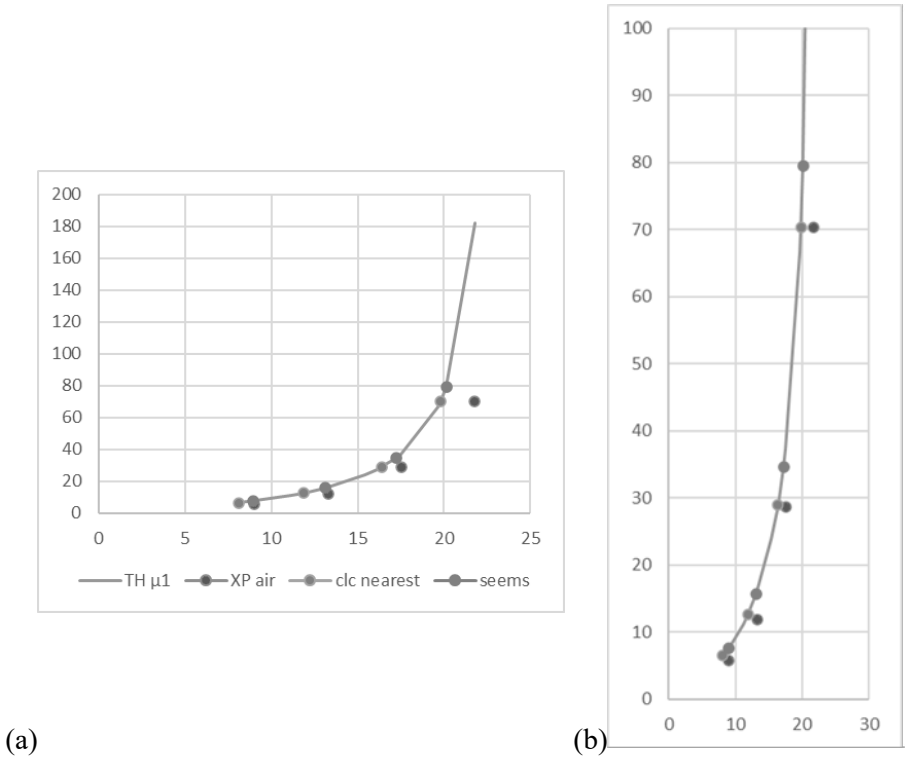


Figure 6: Comparison of Scales. (a) Arbitrary Scales, (b) Identical Scales for Both Axes

Figure 6 demonstrates the proposed method's advantage and correctness. Namely, the relative position of the actual nearest points in Fig. 6(b) looks different from the "seemed" nearest points in Fig. 6(a). Using the proposed effective RMSD, we obtained σ = 3.3% and 1.5% in air and water instead of 19.4% and 26.4%, respectively (i.e., an improvement of 5.8 and 17.6 times).

4: Discussion

The main difference from the theory in Ref. [21] is that we consider the second projection center not partially but fully; also, we use the magnification of period instead of the magnification of coordinate. For the optional screen at the first grid, the moiré magnification can be obtained by multiplication by the coefficient $\frac{\hat{L}-1}{\hat{L}}$:

$$\mu = \frac{\rho(\hat{L}-1)(n\hat{L}-n+1)}{n(1-\rho)\hat{L}^2+(2-n+\rho(2n-1))\hat{L}-\rho(n-1)} \quad (42)$$

The formal difference with the main formula (31) is that $\hat{L}-1$ appears instead of $\hat{L}$ in the numerator.

5. Conclusion

We developed an improved theory of the moiré effect in a parallelepiped filled with a refractive substance. Specifically, we obtained refined formulas for the moiré pattern period. We proposed an improved RMSD estimation method based on the distance to the theoretical curve. We compared the theoretical moiré period with existing experimental data; reliability improved by 5 – 17 times. This study is important for further understanding the dynamic physical properties of the moiré effect with refraction. In practice, the results can be used to measure the refractive index and in advertising.

Declaration of interest. The author declares that no conflict of interest could be perceived as prejudicing the impartiality of the research reported.

Funding. This research received no specific grant from any funding agency in the public, commercial, or not-for-profit sector.

References

1. Amidror, I. (2009). *The Theory of the Moiré Phenomenon: Volume I: Periodic Layers*. Springer Science & Business Media.
2. Saveljev, V. (2022). *The Geometry of the Moiré Effect in One, Two, and Three Dimensions*. Cambridge Scholars Publishing.
3. Yokozeki, S., Kusaka, Y., & Patorski, K. (1976). Geometric parameters of moiré fringes. *Applied Optics, 15*(9), 2223-2227.
4. Bryngdahl, O. (1974). Moiré: formation and interpretation. *Journal of the Optical Society of America, 64*(10), 1287-1294.
5. Dohnal, M. (1999, December). Moiré in a scanned image. In *Photonics, Devices, and Systems* (Vol. 4016, pp. 166-170). SPIE.
6. Sciammarella, C. A., & Chiang, F. P. (1968). Gap effect on moiré patterns. *Zeitschrift für angewandte Mathematik und Physik ZAMP, 19*(2), 326-333.
7. Saveljev, V. (2018). Moiré effect in 3D structures, in Advances in Optics: Reviews, Book Series, Vol 1, Sergey Y. Yurish, Ed., pp. 61-94, International Frequency Sensor Association Publishing. https://sensorsportal.com/advances_in_optics_reviews_vol_1.html
8. Yu, Y., Van Winkle, M., & Bediako, D. K. (2022). Tuning interfacial chemistry with twistronics. *Trends in Chemistry, 4*(10), 857-859.
9. Hennighausen, Z., & Kar, S. (2021). Twistronics: a turning point in 2D quantum materials. *Electronic Structure, 3*(1), 014004.
10. Wang, S., Song, J., Sun, M., & Cao, S. (2023). Emerging characteristics and properties of moiré materials. *Nanomaterials, 13*(21), 2881.
11. Khurana, R. K. (2022). Moiré patterns in nanomaterials. *Materials Science in Semiconductor Processing, 140*, 106406.
12. Latychevskaia, T., Escher, C., & Fink, H. W. (2019). Moiré structures in twisted bilayer graphene studied by transmission electron microscopy. *Ultramicroscopy, 197*, 46-52.
13. Ren, W., Zhu, Z., Zhang, X., Luskin, M., & Wang, K. (2025). Moiré-of-moiré superlattice in twisted trilayer graphene. *Journal of Physics: Condensed Matter, 37*(35), 353001.
14. Oster, G., Wasserman, M., & Zwerling, C. (1964). Theoretical interpretation of moiré patterns. *Journal of the Optical Society of America, 54*(2), 169-175.
15. Karny, Z., & Kafri, O. (1982). Refractive-index measurements by moire deflectometry. *Applied Optics, 21*(18), 3326-3328.
16. Glatt, L., & Livnat, A. (1984). Determination of the refractive index of a lens using moire deflectometry. *Applied Optics, 23*(14), 2241-2243.
17. Fradkin, I. M., Kirtaev, R. V., Mironov, M. S., Grudinin, D. V., Marchenko, A. A., Chugunova, M. M., ... & Volkov, V. S. (2026). Contact Lens with Moiré Patterns for High-Precision Eye Tracking. *Advanced Functional Materials, 36*(29), e22757.
18. Saveljev, V., & Kim, S. K. (2012). Simulation and measurement of moiré patterns at finite distance. *Optics Express, 20*(3), 2163-2177.
19. Saveljev, V., Son, J. Y., Kim, Y., Park, J. G., & Heo, G. (2020). Moiré patterns in non-parallel surfaces such as wedge. *Journal of the Optical Society of America A, 37*(2), 336-345.
20. Saveljev, V., Han, W., Lee, H., Kim, J., & Kim, J. (2020). Moiré effect in double-layered coaxial cylinders. *Applied Optics, 59*(18), 5596-5607.
21. Saveljev, V. (2026, January). Moiré Effect with Refraction. *Photonics, 13*(1), 47.
22. Minimization of scalar function (2026). *SciPy User Guide https*://docs.scipy.org/doc/scipy/reference/generated/scipy.optimize.minimize.html.